11th International Symposium on Turbulence and Shear Flow Phenomena (TSFP11)
Southampton, UK, July 30 to August 2, 2019

IDENTIFICATION OF EFFICIENT FLOW CONTROL STRATEGIES FOR TRUCK MODEL DRAG REDUCTION

Patricia Sujar-Garrido, Marc Michard
Univ Lyon, École Centrale de Lyon,
INSA Lyon, Université Claude Bernard Lyon I,
CNRS, LMFA, UMR 5509,
36 Avenue Guy de Collongue,
F-69134, Ecully, France

Thomas Castelain
Univ Lyon, Université Claude Bernard Lyon I
École Centrale de Lyon, INSA Lyon,
CNRS, LMFA, UMR5509,
43 boulevard du 11 novembre 1918,
F-69100, VILLEURBANNE, France

Yann Haffner
Institut Pprime, UPR3346,
ENSMA-Université de Poitiers, Futuroscope, France

ABSTRACT

This study presents the modifications produced in the controlled wake of a square-back blunt truck model using unsteady pulsed jets combined with small flaps, and the corresponding mean base pressure changes. Different control strategies obtained using different locations of the pulsed jets around the model base are considered. A base pressure increase is obtained for a variety of control strategies implying one to four edges used in a synchronized manner. The vertically-asymmetric forcing excluding the bottom edge results in 33% increase of the mean base pressure and 28% reduction of the wake length with a reduced energetic cost with respect to the forcing strategy involving the four model edges. This control strategy also proves to be efficient in yawed configurations (5°).

INTRODUCTION

Drag reduction on truck models by actuation of the near wake has been previously studied, on the basis of continuous blowing (Englar (2005)), pulsed (Szmigiel (2017); McArthur *et al.* (2016); El-Alti *et al.* (2016)), or synthetic jets (Chaligné (2013)) located at the edges of the model's base. These jets emerging from rectangular slits with an angle of 45° or aligned with the main flow provide control authority on the near wake. The actuation was possibly coupled with rounded or curved flaps, which allows for efficient wake modifications leading to base pressure recovery. Actuation was performed either all around the base (El-Alti *et al.* (2016); Englar (2005)), on the top edge only (Chaligné (2013)) or on the side and top edges (Szmigiel (2017)). The peculiarity of the wake of model trucks is a notable dependence on the underbody velocity as shown by Castelain *et al.* (2018). In real-world application, this is influenced by the trailer underbody geometry and the tractor-trailer combination for instance. This result is reminiscent of that obtained by Grandemange *et al.* (2013) when changing the model ground clearance. The underbody velocity thus directly influences the wake structure, which is notably different from that of a the square-back Ahmed body wake (Barros *et al.* (2016)) and the efficient strategies for its control may differ from that previously identified for square-back Ahmed bodies. For control cost reduction as well as promotion of the dynamic interaction between the control jets and the main flow, high frequency forcing far above the characteristic frequencies of the natural flow instabilities is of practical interest. In the following, the actuation method consists in pulsed jets at a fixed actuation frequency and is applied to an adapted simplified truck model, representative of long-hauls. When considering the variety of control strategies applied so far on truck models and in particular the location of the active slits, the present approach aims at determining the efficiency of various strategies on the considered truck model and identifying the main features of the most efficient ones.

EXPERIMENTAL SET-UP

The results presented here are derived from experiments performed in the S620 closed-loop wind-tunnel at Pprime. A sketch of the mock-up is given in Figure 1. This illustrates the main geometrical features of this simplified truck-model, namely its height H=0.36 m, its width W=0.3m and the presence of side skirts which sets a constant ground clearance G with respect to the non-moving floor. An adaptable head loss device consisting in a 20mm-thick grid is located in the underbody. The porosity ϕ of the grid can be varied such that the maximum velocity in the underbody flow ranges from 0 to U_∞. The model is mounted on a motorized circular plate integrated in the floor, to adjust the yaw angle between the free stream velocity and the model vertical sides.

In the following, the non-dimensional lengths, denoted by a $\star$ symbol, are relative to the model height H. The model ground clearance $G^\star$ is set to 0.25. The velocity is non-dimensioned by the free stream velocity U_∞, set to 25 m.s^{-1}. The corresponding Reynolds number is $Re_H = 5\ 10^5$.

Time-averaged pressure measurements are allowed by flush-mounted pressure taps (64) distributed over the mo-

del nose (13), sides (16) and base (35). The recording are performed using a miniaturized pressure scanner integrated in a DTC Initium environment and a National Instrument PXIe-8820 acquisition unit, at 200 Hz and over 20 seconds per point at least. Time-averaged pressure coefficient $\overline{C_p}$ and its spatial average on the model base $< C_p >$ are reported here. The base pressure change under control conditions is depicted by an indicator γ_p defined by the ratio between the mean base pressure in a controlled case to that of the reference configuration, without control.

$$\overline{C_p} = \frac{\overline{p} - p_\infty}{\frac{1}{2}\rho U_\infty^2}; \qquad \gamma_p = \frac{< \overline{C_p} >}{< \overline{C_p^{\text{ref}}} >} \tag{1}$$

A 2D2C PIV system is used to measure the velocity fields in the vertical mid-plane for different control strategies. Moreover, to capture the effects of the control in static-yaw conditions, acquisitions in the horizontal mid-plane are also performed.

Actuation is performed by unsteady pulsed jets generated by solenoid valves fed with compressed air and driven by a 4-channel dedicated electronics. Rectangular exit slits of 1mm-thickness are distributed over each of the 4 model-edges. The pulsed jets exit over 20 mm length 25° inclined flaps flush-mounted to the slits. To allow various control strategies using only parts of the available slits, the driving electronics is designed such that the slits distributed over one given edge can be actuated independently from the others. Hot-wire measurements performed at the slit exit are used to determine the velocity amplitude $V_{\max}$ of the control jets during the blowing phase, hence to define the momentum coefficient C_μ defined as :

$$C_\mu = \text{DC}\, N \frac{s_j}{WH}\left(\frac{V_{\max}}{U_\infty}\right)^2 \tag{2}$$

with DC the duty-cycle of the valves driving signal, s_j the area of a single slit and N the number of slits used in a given control strategy. As previously shown by Michard *et al.* (2017), the velocity amplitude of the unsteady jets is strongly related to the forcing frequency f, as a result of the acoustic resonance of the pneumatic line from the valve to the slit exit. In the present study, the actuation frequency corresponds to the resonance frequency of the system, which is close to 350 Hz. For a given pressure of the compressed air, this actuation frequency allows a maximum unsteady shear between the control jets and the main flow. These high blowing velocities are compensated by a suction phase with negative velocities at the slit exit, due to the existence of acoustic waves of high amplitude. Therefore working at the acoustic resonance frequency allows to reach large C_μ for moderate compressed air consumption, in comparison to other actuator working frequencies.

RESULTS

In the following, the time-averaged pressure coefficient as well as wake characteristics captured in vertical and horizontal model mid-planes are commented together, for different actuation strategies. First, the main features of the effects of the control performed along the 4 model-edges, referred to as *global forcing*, are depicted. Secondly, selected results for various control strategies are commented.

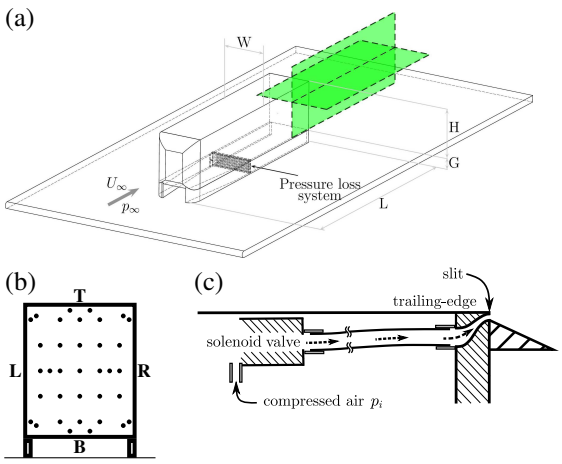

Figure 1. Sketch of the simplified truck model. Side view of the set-up (a), rear-view including the pressure taps location and the name of base edges used for the different control strategies (b) and details of the control system (c)

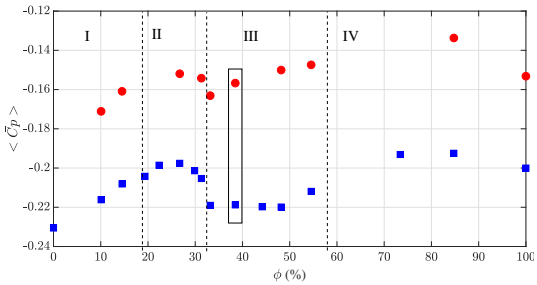

Figure 2. Evolution of the spatially-averaged mean base pressure $< \overline{C_p} >$ with porosity ϕ, for the reference case (■) and global forcing (•)

Reference configuration and global forcing

The evolution of the time-averaged mean coefficient $< \overline{C_p} >$ with the porosity of the grid placed in the model underbody, which drives the underbody flow magnitude, is provided in Figure 2. Two configurations are considered: the reference case without control and the global forcing case for a given actuation momentum coefficient (C_μ = 3.2 10^{-2}) and frequency (f = 350 Hz). First, for the reference case, there is a marked evolution of $< \overline{C_p} >$ with ϕ with a noticeable drop $< \overline{C_p} >$ for a grid porosity between 30% to 40%. This behavior recalls the properties highlighted by Grandemange *et al.* (2013) and Castelain *et al.* (2018), for the evolution of the same parameter with the ground clearance and with the underbody mean velocity respectively. Castelain *et al.* (2018) identified four flow classes as ϕ ranges from 0 to 1, and designated as class (III) the wake structure leading to the constant value of $< \overline{C_p} >$ obtained in the range $\phi \in [30\% : 55\%]$.

Interestingly, the behavior observed in the reference case still holds for the controlled case. This implies that the effects of global forcing correspond, at first order, to a shift in base pressure independently from the class type. Thus, the control apparently preserves the class type for a given reference flow; a proper identification of flow classes would nevertheless require the application of the analyses presented by Castelain *et al.* (2018), which is beyond the scope of the present paper. Instead, the analysis will focus

in the following on a fixed grid porosity of $\phi = 38\%$, which corresponds to a class (III) flow chosen because of its similarity with real long-haul vehicles configurations. The mean wake in this configuration is depicted in Figure 3, for both the reference and the controlled cases, in the vertical mid-plane. A major difference with the well-documented case of a Ahmed body is clearly noticeable: With respect to the well-documented wake of a Ahmed body associated with a recirculation bubble attached to the four base edges and surrounded by a potential flow, a major difference obtained here is that the low underbody flow momentum prevents such a recirculation bubble to form in the wake. Considering the non-moving ground condition used here, the wake is thus marked by the detachment from the ground of this low-momentum underbody flow. This leads to an interaction of the resulting curved jet and the shear layer developing from the model roof. It has previously been shown in Castelain *et al.* (2018) that the curvature of this jet also depends on the value of ϕ. When applying the control over the four base edges, the global structure of the wake is not modified but the upper shear layer is deflected toward the ground and the curvature of the jet from the underbody flow is higher. This implies that its interaction with the upper shear layer appears closer to the base.

Influence of the momentum coefficient on mean base pressure

Different control strategies are evaluated here. A given control strategy consists in actuating over combinations of 1 to 4 base edges: the top (T), bottom (B), left (L) and right (R) edges. In the following, a simplifying notation is used and illustrated by the following example: (LB) refers to the control strategy implying the active slits located on the left (L) and bottom (B) edges. The evolution of normalized pressure recovery γ_p with the control jets momentum coefficient for different control strategies is presented in Figure 4. For a given strategy, the values tested for C_μ were obtained either by varying the input pressure in the pressurized air tank located in the model or by changing the duty-cycle. Because of the different tested strategies do not imply the same number of active base edges, which ranges from 1 (single edge control) to 4 (global control), the momentum coefficient per unit active slit C_μ/N is here considered. It appears that the pressure recovery reaches a constant value for a sufficiently high value of C_μ/N estimated here around 1.2×10^{-3}. In the following, the results will correspond to fixed tank pressure and duty-cycle corresponding to this value of C_μ/N.

Efficiency of control strategies

Figure 5 gives the base pressure recovery obtained in such conditions, for various control strategies and a model aligned with the flow (fig. 5(a)) or with a yaw angle of 5° (fig. 5(b)). From a general viewpoint, one may expect that for a given value of C_μ/N, an increase in the number of active slits N would lead to an increase in the model's time averaged base pressure (a decrease in γ_p), mainly because the control would then concern a larger fraction of the base. This crude expectation is balanced by the fact that the initial model wake development is dominated by the development of four shear layers detaching from the four model edges. Each of these shear layers probably has a specific response to the control, considering for instance the difference in momentum between the top and bottom shear layers or the fact that the early interaction between the top shear layer and bottom shear layer, mentioned previously, does not exist between the side shear layers. The interpretation of the link between the changes in wake characteristics due to global forcing and the resulting base pressure distribution is rather complex, but distinguishing between the effects of the control on each shear layer is probably even harder. Three dimensional interactions between two neighboring shear layers appearing downstream of the model base or interactions between two facing shear layers are expected such that, for instance, the base pressure change obtained with (LB) will not necessarily correspond to that obtained with (L) added to the change associated with (B) only. Nevertheless, considering first the results for the unyawed model, the fixed value for C_μ/N imposes simply four sets of values of C_μ between 10^{-2} to 4.10^{-2}, because N corresponds to the number of slits along one to four base edges. The general trend of a decrease in γ_p is observed, but there is a large deviation in pressure recovery between the strategies implying the same value of N. For instance, for a given control cost, (BR) - respectively BLR - appears much less efficient than (TR) - respectively TLR. The strategies implying the slits located on the top edge (T, TR, TB, TLR, TLRB) bring more base pressure recovery than the others. Additionally, the value for γ_p obtained with the control strategy (T) compares well to that obtained with a similar strategy by Chaligné (2013), but with synthetic jets on top and lateral flaps with smaller angle. Moreover, the most effective control strategy (TLR) differs from global forcing: not only the control cost is less by a factor roughly equal to 1.3, but the pressure recovery is in itself greater by 5% (see arrow (i) in Fig.5(a)) . This raises the question of the effect on the wake of the control on the bottom edge of the model base. This effect is clearly disadvantageous as the control is applied on the other edges (TLRB), but also in almost all the other configurations tested. For instance, (B) is detrimental to base pressure recovery, since γ_p=1.02 in this case; interestingly, the difference between (T) and (TB) is also of 2% (see arrows (ii)). Additionally, if the bottom edge slits are used in combination of side edges, passing from the (LR) to (LRB) (and equivalently from (R) to (RB), see arrows (iii)) brings a penalty even higher, around 3 to 5%, which is close to the difference obtained earlier between (TLR) and (TLRB). This nearly constant effect of the control on the bottom edge requires further analyses to be presented in the next section. Positive interaction effects between two facing shear layers are also obtained. Indeed, even if the comparison between (T) and (TB) proved that the resulting interaction does not help in increasing the mean base pressure, the comparison between (R) and (LR) provides a different result. For symmetry reasons in the case of figure 5(a), it is expected that (L) would provide the same base pressure recovery as that given by (R), which is almost zero. The combination of the two actuations (LR) provides nevertheless a decrease in γ_p around +7% (see arrows (iv)), while preserving the mean symmetry condition around the vertical mid-plane occurring in the reference flow.

The configuration with a yaw angle of 5° (fig.5(b)) is now considered. The main features obtained in the case of a model aligned with the flow (fig.5(a)) are retrieved in this case, as for instance the properties highlighted by arrows (i) and (ii). The asymmetry introduced by the yawing condition results in a clear difference between the results obtained with (R) or (L) only, and similarly with (TR) or (LR) (see arrows (v)). The control implying the windward side

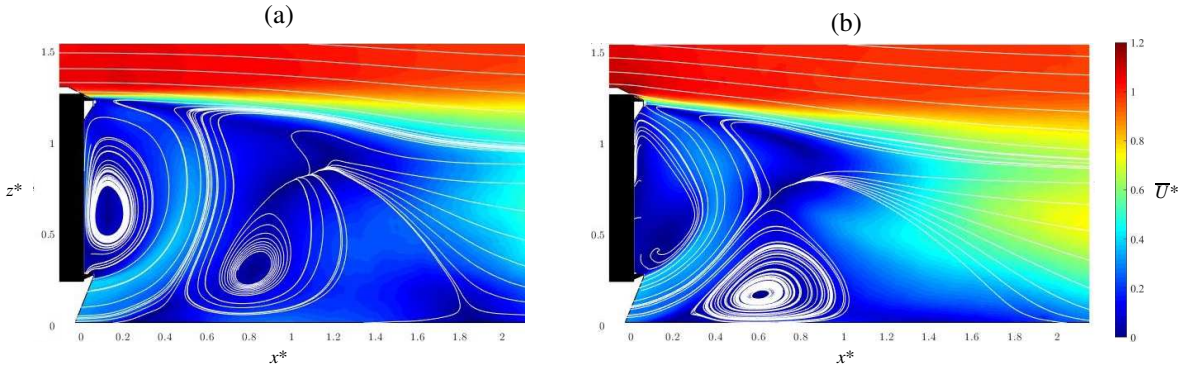

Figure 3. Time-averaged velocity in the vertical mid-plane, for the reference configuration (a) and global forcing (b)

(R or RT) is much more efficient than that concerning the leeward side (R or RT), which is consistent with previous results obtained by Li *et al.* (2019). Interestingly, (RT) provides a pressure recovery close to that obtained with the global forcing in this case, but at half the control cost. Further analyses are provided hereafter using maps of base pressure and of time-averaged velocity in the horizontal mid-plane.

Base pressure and velocity maps for selected control strategies

The examination of base pressure maps complements here the previous analysis based on relative spatial averaged values γ_p. Because configuration at yawing condition is considered, PIV in the horizontal plane will be examined when available in relation with the corresponding pressure map for the most promising control strategy in terms of γ_p, namely global forcing (TLRB), (TLR) and (TR).

Model at zero yaw angle The pressure maps and mean velocity in horizontal mid-plane are given in Figure 6. Both for time-averaged base pressure and velocity, the results for the reference case exhibit a symmetry with respect to the vertical mid-plane; this symmetry condition is also fulfilled by the results obtained for (TRLB) and (TRL). In these two cases, the two recirculation zones are closer to the base, such that their pressure footprint are more pronounced than in the reference case. Consequently, the pressure distribution in these cases slightly deviates from a marked horizontal stratification as noticed in the reference case. The (TR) strategy imposes a strong asymmetry in the base pressure distribution, which results from the asymmetry in the corresponding controlled wake. A pressure deficit is noticeable next to the controlled side, particularly the bottom edge. For this case, the lateral side shear layers are not deflected in a similar fashion one from the other; the shear-layer from the controlled edge (R) is notably deflected, in the same way as what happens in (TRLB) or (TRL), while the shear-layer from the non-controlled edge (L) seems to behave as in the reference case. To go further, Figure 7(a) depicts the streamlines originating from one given point next to the base edges ($|y^*| = 0.4$) for the four control strategies. This confirms that in their early development stages and up to $x^* \geqslant 0.5$, the lateral shear-layers are directly driven by the applied control. One may note that the longitudinal distance up to which these similarities occur probably depends on the height between the floor and the observed horizontal plane in which the streamlines are evaluated. Considering the strategies where the right edge slits are active (TRLB, TRL, TR), the streamlines exhibit a good fit, so as for the strategies where the left edge slits are active (TRLB, TRL). For the strategy that does not use the left edge slits (TR), the results are very similar to that obtained in the reference case. Interestingly, complementary conclusions can be derived from Figure 7(b) which exhibits the longitudinal evolution of the maximum of the 2D turbulence intensity k^*. For clarity, only one curve is presented for symmetric flows (reference case, TRL); two curves are presented for the (TR) strategy. The curve corresponding in this case to the maximum levels of k^* in the shear layer downstream of the right edge is very similar to that obtained with the (TRL) strategy; the curve representing the maximum levels on the other side of the model (no control) nevertheless differs from that of the reference case, at least for $x^* \geqslant 0.5$. Finally, to compare the (TRLB) and (TRL) strategies, one uses again Figure 7(a) to indicate that the two sets of streamlines obtained in these cases are very close to each other. The longitudinal location for which a significant difference occurs between these streamlines is around x^*=0.8, which is related to 3D effects resulting from the wake closure. It is thus postulated that this difference in wake closure may come from a change in the orientation of the curved jet forming from the underbody exit due to the control applied (TRLB) or not (TRL) on the bottom edge. As shown in Figure 3, the jet curvature is less pronounced as the bottom side is not controlled. A parallel can be drawn with the case of a slightly higher value of the porosity Φ, which would provide more momentum to the underbody flow and thus a reduced curvature. In this case, as indicated in Figure 2, the base pressure recovery would be slightly higher, starting from the reference point of Φ=38% and comparing the controlled and reference values for slightly higher Φ.

Model at 5° yaw angle The changes in base pressure and velocity fields brought by the control strategies (TRLB), (TRL) and (TR) are displayed in the case of a 5°-yaw configuration. The reference case exhibits an asymmetric base pressure distribution with respect to y^*=0, with a low-pressure area marked on the leeward side. This asymmetry is associated with the noticeable recirculation area in the near wake, also on the leeward side. Interestingly, the low-pressure footprint is attenuated with the (TRLB) control strategy, and even more with the (TRL) strategy which is again the most efficient for base pressure recovery. This result is consistent with the findings of Li *et al.* (2019). (TR) imposes again a global increase of the base pressure with respect to the reference case, but contrarily to the two previous strategies, a pressure deficit occurs on the windward side. This pressure map is very close to that obtained in the unyawed case, which is interpreted as the consequence of the orientation of the model's wake. Indeed in this case, it

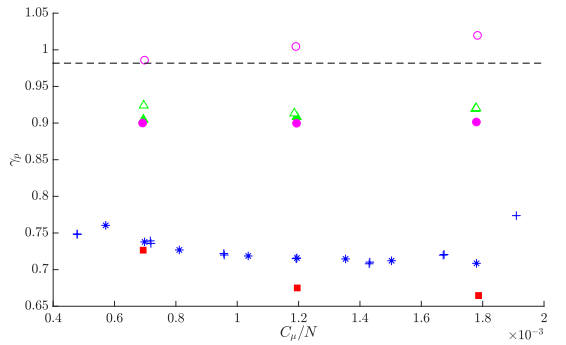

Figure 4. Gain γ_p in time-averaged base pressure with control jets momentum coefficient, for different control strategies: T (•), B (○), TB (▲), LR (△), LTR (■), LRTB - global forcing (blue symbols)

is well aligned with the unperturbed flow in comparison to the other cases (reference, TRLB or TRL), and there is a striking similarity with the result obtained for the 0° yaw configuration.

Conclusion

The efficiency of flow control strategies for truck model drag reduction based on pulsed jets at high frequency coupled with 25° inclined small flaps has been asserted by considering the changes on mean average base pressure. Most of the strategies tested bring a base pressure recovery, the model being either aligned with the main flow or at a yaw angle of 5°. The strategies implying actuation on the top base edge are more efficient, with a maximum efficiency corresponding to actuation on the top and the lateral sides (TRL) rather than a global forcing using the four sides simultaneously. A first interpretation of this result consists in considering the changes brought to the orientation of the underbody flow by actuating on the bottom side, whose effects ressemble to a change in the underbody model porosity. Further investigations on the basis of PIV measurements in the vertical mid-plane for the concerned control strategies would help in confirming this interpretation.

ACKNOWLEDGEMENTS

This work is performed within the program Activ_Road (ANR-15-CE22-0002) operated by the French Agence Nationale de la Recherche (ANR) and in the framework of the Labex CeLyA of the Université de Lyon, within the programme "Investissements d'Avenir" (ANR-10-LABX-0060/ANR-16-IDEX-0005). The authors want to thank the support during experimental campaigns by J.-M. Breux, F. Paillé, P. Braud, R. Bellanger and E. Jondeau.

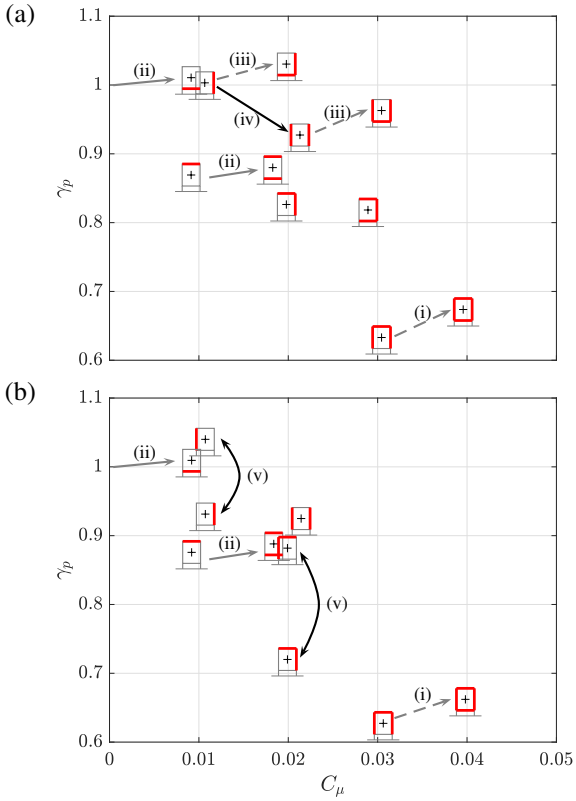

Figure 5. Pressure recovery γ_p with C_μ for different control strategies. Model aligned with the main flow (a) and with a yaw angle of 5° (b). Each value (+) is associated with a marker representing the base edges slits used for the control (red segments).

REFERENCES

Barros, D., Borée, J., Noack, B. R., Spohn, A. & Ruiz, T. 2016 Bluff body drag manipulation using pulsed jets and coanda effect. *J. Fluid Mech.* **805**, 422–459.

Castelain, T., Michard, M., Szmigiel, M., Chacaton, D. & Juvé, D. 2018 Identification of flow classes in the wake of a simplified truck model depending on the underbody velocity. *Journal of Wind Engineering and Industrial Aerodynamics* **175**, 352–363.

Chaligné, S. 2013 Contrôle du sillage d'un corps non profilé. application expérimentale à une maquette simplifiée de véhicule industriel. PhD thesis, ECL - No. 2013-50.

El-Alti, M., Chernoray, V., Kjellgren, P., Hjelm, L. & Davidson, L. 2016 Computations and full-scale tests of active flow control applied on a volvo truck-trailer. In *The Aerodynamics of Heavy Vehicles III. Springer*, pp. 253–267.

Englar, R. J. 2005 Improved pneumatic aerodynamics for drag reduction, fuel economy, safety and stability increase for heavy vehicles. *SAE Tech. paper* **2005-01-3627**.

Grandemange, M., Gohlke, M. & Cadot, O. 2013 Bistability in the turbulent wake past parallelepiped bodies with various aspect ratios and wall effects. *Phys. Fluids* **25**, 095103.

Li, R., Borée, J., Noack, B.R., Cordier, L. & Harambat, F. 2019 Drag reduction mechanisms of a car model at moderate yaw by bi-frequency forcing. *Physical Review Fluids* **4**, 034604.

McArthur, D., Burton, D., Thompson, M. & Sheridan, J. 2016 On the near wake of a simplified heavy vehicle. *Journal of Fluids and Structures* **66**, 293314.

Michard, M., Sesmat, S., Castelain, T., Jondeau, E., Bideaux, E. & Bourgeois, A. 2017 Unsteady pulsed jets using pneumatic valves for flow separation control: effect of internal acoustic waves on external flow structure. In *GdR Contrôle des écoulements, Orléans, 8-9 nov.*.

Szmigiel, M. 2017 Effet du flux de soubassement sur la dynamique du sillage d'un corps non profilé à culot droit. application du contrôle actif pour la réduction de traînée de véhicule industriel. PhD thesis, ECL - 2017LYSEC16.

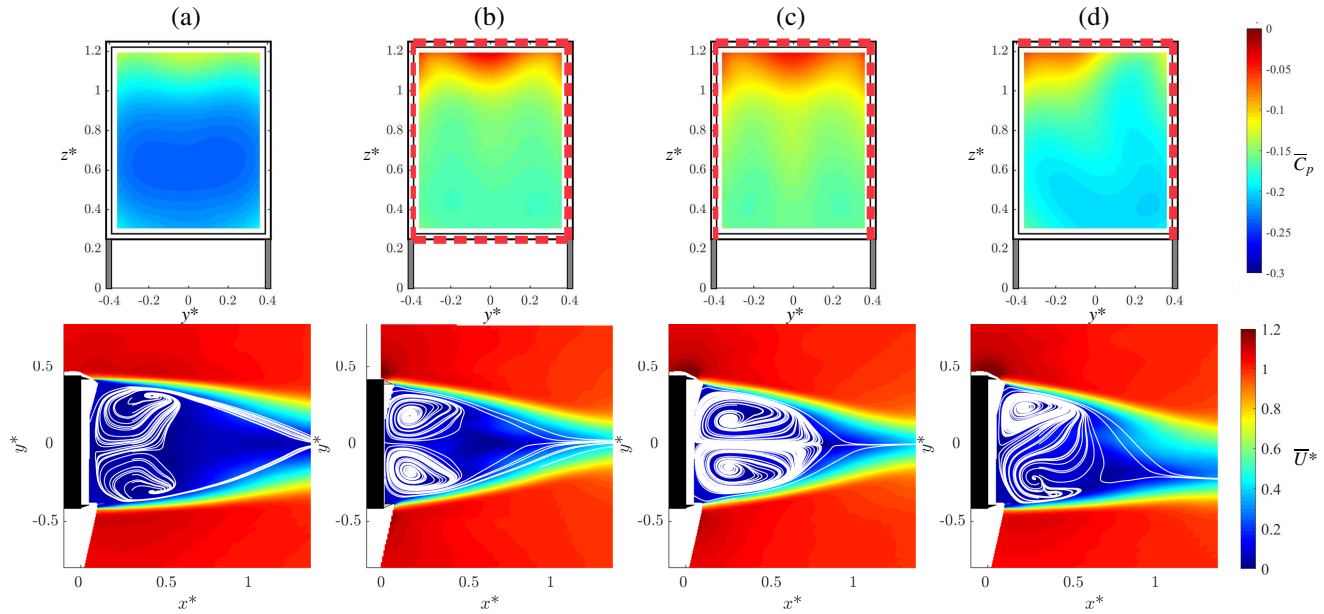

Figure 6. Time-average pressure coefficient $\overline{C}_p$ and velocity magnitude in the horizontal mid-plane for reference case (a), global forcing TLRB (b), TLR (c) and TR (d). Red dashed lines illustrate the active edges for the applied control strategy. White lines correspond to streamlines superimposed on the velocity maps. Model at yaw angle 0°

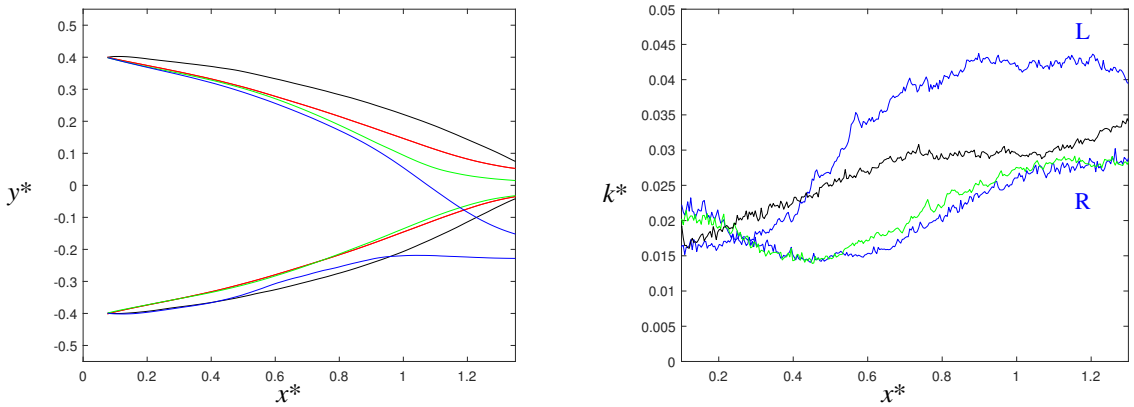

Figure 7. Streamlines for a given starting point next to the model lateral edges (a) and axial evolution of maximum value of 2D turbulence level k^* (b) in the horizontal mid-plane, for the reference case (black) and different control strategies: TRLB (red), TRL (green) and TR (blue)

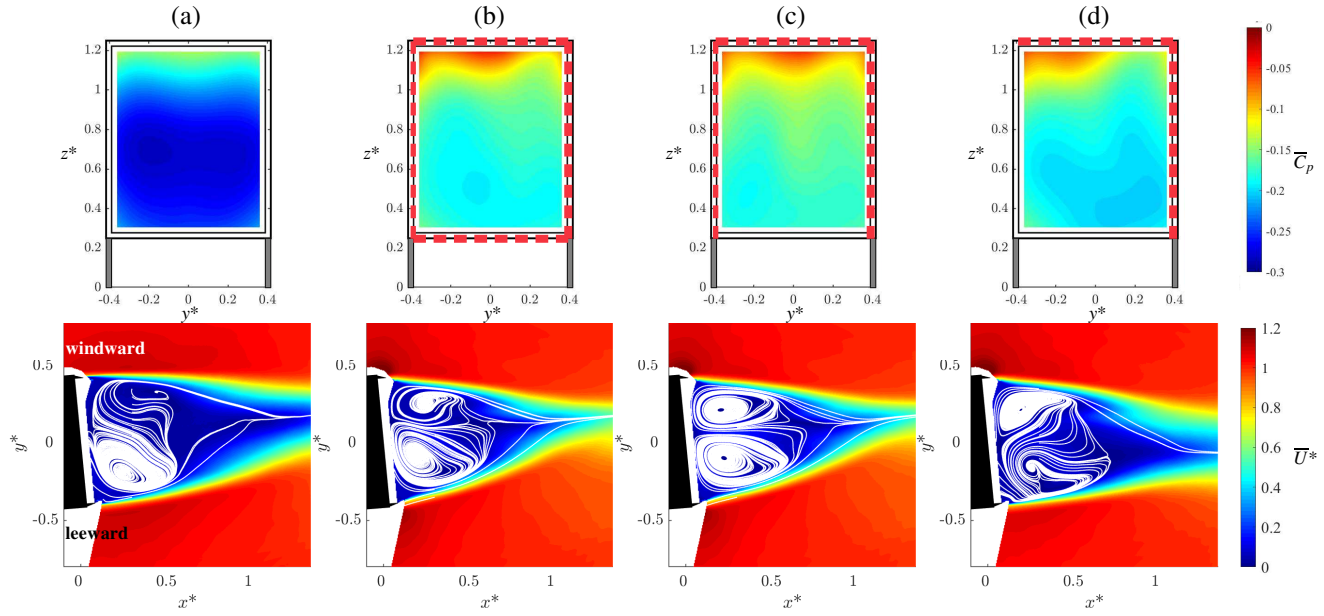

Figure 8. Same legend as Figure 6. Model at yaw angle 5°